ACS NANO

www.acsnano.org

ARTICLE

Reversible Morphology Locking via Metal Infiltration in a Block Copolymer

Mingchao Ma, Runze Liu, Tingyu Su, Zehao Sun, and Caroline A. Ross*

Cite This: *ACS Nano* 2023, 17, 12225–12233

Read Online

ACCESS | Metrics & More | Article Recommendations | Supporting Information

ABSTRACT: **Metal infiltration from an acid solution of a metal precursor into the poly(2-vinylpyridine) (P2VP) microdomains of a polystyrene-*b*-P2VP block copolymer is shown to reduce the uptake of solvent vapor during a subsequent solvent annealing process, locking the morphology of the self-assembled microdomains. The amount of metal, here Pt, incorporated into the P2VP increases with both metal precursor $[PtCl_4]^{2-}$ and hydrochloric acid concentrations, reaching 0.83 Pt atom per pyridine unit. The metal is then exfiltrated using a KOH + ethylenediaminetetraacetic acid disodium salt dihydrate (Na_2EDTA) complexing solution, which restores solvent uptake and unlocks the morphology. The reversibility of the metal infiltration and morphology locking is demonstrated in a multistage annealing process and is confirmed for Fe as well as Pt. Reversible locking and unlocking of block copolymer microdomain morphologies expand their utility for nanofabrication processes by allowing the morphology to be fixed during subsequent process steps.**

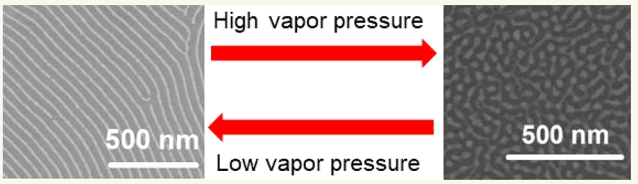

KEYWORDS: *self-assembly, block copolymer, metal infiltration, metal exfiltration, reversible morphology*

Block copolymers are useful for nanofabrication and pattern transfer due to their ability to self-assemble into ordered nanostructures with feature sizes of a few nm and above.[1−5] The equilibrium bulk morphology of a diblock copolymer (BCP) comprises spheres, hexagonally packed cylinders, gyroids, or lamellae, determined by the Flory−Huggins interaction parameter (χ), degrees of polymerization (N), and volume fractions (f) of the constituent blocks.[6−8] However, nonbulk morphologies may also be obtained, *e.g.*, by choice of the annealing method,[9−11] by confining the BCP as a thin film or other geometry,[12−14] by controlling its interfacial or surface chemistry,[15−17] or by substrate templating.[18−20] Processing methods that can switch between morphologies or vary the orientation of the microdomains endow BCPs with additional functionalities in nanofabrication.

Solvent vapor annealing (SVA), in which a BCP film is exposed to solvent vapor to lower the effective interaction parameter (χ_{eff}), increase the chain mobility, and facilitate microphase separation,[21−28] can produce multiple morphologies from one BCP through selective swelling in the solvent vapor. The swelling ratio (the ratio of swelled thickness to original thickness), χ_{eff}, and the resulting morphology are determined by the annealing conditions, which include solvent composition,[25,29−31] vapor pressure,[32−34] temperature,[9,35−37] and humidity;[38−40] they also depend on the composition of the blocks.[41,42] As an example, Jeong and co-workers utilized different solvent vapors to produce spherical, cylindrical, and perforated lamellar morphologies from a poly(2-vinylpyridine)-*b*-poly(dimethylsiloxane) (P2VP-*b*-PDMS) BCP thin film.[25] Successive SVA processes using different solvents or vapor pressures can switch the morphology, *e.g.*, from spherical to cylindrical, in polystyrene-*b*-poly(dimethylsiloxane) (PS-*b*-PDMS).[42] However, during an SVA process, it is difficult to restrict morphological changes to selected regions of the BCP film and, therefore, to accomplish changes in morphology in specific locations.

Cross-linking[41−47] provides a strategy to lock the microdomain morphology and prevent reorganization during successive annealing processes. Various cross-linking methods have been used; for example, PS-*b*-PDMS has been cross-linked by physical collisions with energetic Ar atoms[41] and by electron-beam irradiation,[42] and poly(α-methylstyrene)-*b*-poly(4-hydroxystyrene) was cross-linked by exposure to ultraviolet light, locking the structure of the exposed region during subsequent annealing.[44] These chemical cross-linking processes are effective in locking the structure, but they are not reversible.

Infiltrating metal to bind with one or more copolymer blocks modifies the composition of the blocks, which can leave metal

Received: January 24, 2023
Accepted: June 16, 2023
Published: June 26, 2023

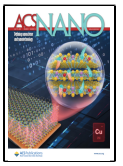

https://doi.org/10.1021/acsnano.3c00723
ACS Nano 2023, 17, 12225−12233

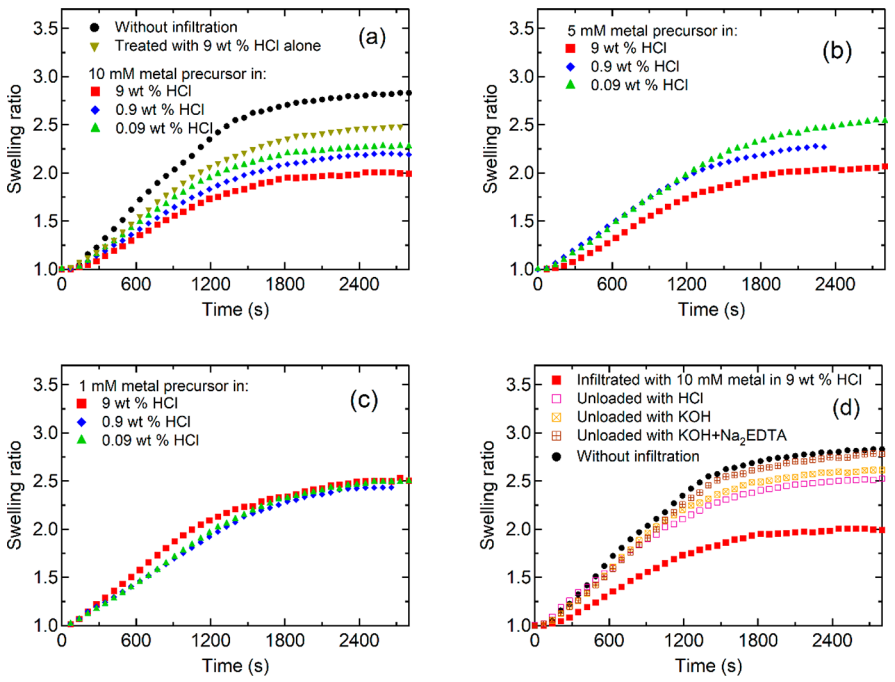

Figure 1. Swelling ratio of PS-*b*-P2VP block copolymer thin films in chloroform by the constant flow method: (a−c) Films infiltrated by (a) 10 mM, (b) 5 mM, and (c) 1 mM metal precursor solution with HCl of different concentrations. (a) Swelling ratio of the as-cast film without infiltration and a film treated with HCl without metal salt. (d) Infiltrated film (same as red data in (a)) is unlocked by solutions of HCl, KOH, and Na_2EDTA.

patterns after etching,[48−51] as well as introducing electrostatic interactions between the chains. P2VP or poly(4-vinylpyridine) (P4VP) blocks have been widely used in an infiltration process[52−55] in which protonated pyridine groups (which accept a proton from the acid due to their Brønsted base character) bind with anionic metal complexes such as $[PtCl_4]^{2-}$ or $[Fe(CN)_6]^{3-}$ from an aqueous acidic solution via electrostatic interactions.[48,56] This is reported to produce mushroom-like protrusions of the vinylpyridine block through the majority PS that provide channels for metal infiltration.[48,52] Metallization and etching of annealed PS-*b*-P2VP or PS-*b*-P4VP films therefore produce a chemically and topographically inhomogeneous surface, which can guide the assembly of a subsequent BCP layer, forming multicomponent metallic meshes or hierarchical dot/line patterns.[24,54] Compared to P4VP, the stronger steric interactions between the nitrogen lone pair and the backbone in P2VP constrains the binding of P2VP with other species, especially large species, which is expected to result in lower metal infiltration of the pyridine groups.[57] Subsequent immersion in HCl was shown to unload metal from the pyridine blocks.[58] Prior work on metal infiltration into BCPs has generally focused on the formation and characterization of the resulting metal nanostructures,[24,48−56,58−61] and the locking effect of metal infiltration on subsequent morphological evolution during annealing and its unlocking via metal removal (exfiltration) remain to be elucidated.

In this work, we show that even low concentrations of infiltrated metal dramatically reduce the swelling ratio of PS-*b*-P2VP thin films, demonstrating a locking effect on the morphology. The swelling ratio is then restored to match that of the pristine film by unloading the metal using a complexing agent, unlocking the morphology, and allowing chain reorganization. Multiple cycles of solvent annealing applied to locked and unlocked films demonstrate selective control over the morphology, and the amount of metal incorporated into the films is quantitatively analyzed after locking and unlocking. This work provides a process for reversible manipulation of the morphology of a BCP film.

RESULTS AND DISCUSSION

Metal Infiltration and Its Effect on Swelling Ratio in a Solvent Vapor. The swelling ratio of the BCP film provides a diagnostic indicator of the locking effect of metal infiltration (Figure 1a−c). A low swelling ratio, SR, compared to that of the as-cast film indicates that rearrangement of the chain configurations is impeded and the morphology is locked.

The as-cast film (black dots, Figure 1a) has a saturation SR of 2.89 in chloroform vapor in the constant flow annealing chamber (Methods), but for metallized films, the electrostatic charging of the P2VP chains caused by protonation and metal infiltration limits the uptake of chloroform vapor and lowers the SR. The effect of metal infiltration on SR depends on both the metal concentration and the acid concentration in the solution. When the metal precursor concentration was 10 or 5 mM, the SR decreased with increasing HCl concentration, indicating that HCl concentration was the major factor determining the amount of metal uptake. However, for 1 mM metal precursor, SR had little dependence (less than 3% variation) on HCl concentration; that is, for these low metal concentrations, metal precursor concentration was the major factor determining the metal uptake.

To quantitatively analyze these trends, the swelling curves were fitted by the Kohlrausch−Williams−Watts function (Methods), which provides an excellent empirical fit exemplified by Figure S1. The fitting parameters are summarized in Table 1. τ falls in the range of 1000−1200 s, and β varies within the range of 1.27−1.81. These parameters

https://doi.org/10.1021/acsnano.3c00723
ACS Nano 2023, 17, 12225−12233

Table 1. Fitting Parameters of Swelling Curves during Solvent Annealing[a]

Metal precursor concentration (mM)	HCl concentration (wt %)	$A + 1$	τ (s)	β
0	0	2.89	1199	1.64
10	9	2.01	1036	1.73
	0.9	2.23	1100	1.57
	0.09	2.28	992	1.62
5	9	2.05	1084	1.81
	0.9	2.32	1013	1.50
	0.09	2.44	1102	1.27
1	9	2.53	1041	1.44
	0.9	2.48	1184	1.55
	0.09	2.56	1224	1.57

[a]The coefficient of determination (R^2) of every fitting is higher than 0.99.

do not vary systematically with the concentration of the metal or acid. τ and β represent the characteristic time for the SR to equilibrate and the width of the SR curve, respectively,[62−64] and are governed by the chamber volume, geometry, and gas flow rate rather than by solvent transport within the BCP film. However, $A + 1$, the plateau value of SR, varies with both the metal precursor concentration and HCl concentration during metallization, as illustrated in Figure 2.

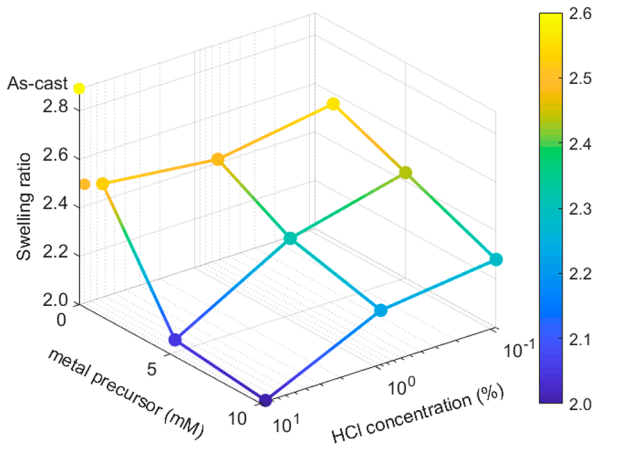

Figure 2. Swelling ratio plateau of metal-infiltrated PS-*b*-P2VP thin films. The point at SR = 2.89 on the vertical axis represents the unmetallized pristine film, and the independent point at SR = 2.49 represents the film treated with 9 wt % HCl without metal precursor.

Table 1 shows that the SR of all the metal-infiltrated films is less than the SR of the as-cast film. SR decreases with increasing concentration of both metal and HCl, indicating that the infiltration process suppresses solvent uptake. However, even for the largest concentrations of metal precursor and HCl, the SR only decreased to 2.01. The modest change in SR upon metallization is likely because the metal is infiltrated only in the P2VP block, and the PS, which constitutes the majority block, is still able to swell in the chloroform vapor. Nevertheless, we will show that the locking of the P2VP microdomains by metal infiltration is effective in preventing morphological changes during SVA.

Figure 3a,b present a STEM cross-section image of a 37 nm thick film after infiltration, which illustrates the Pt distribution. In the high-angle annular dark field (HAADF) image, Pt infiltration increases the contrast between two blocks and reveals a single-layer cylindrical structure with a periodicity of ∼ 50 nm. The EDS image (Figure 3b) reveals Pt within the cylindrical P2VP domains, similar to other reports.[55,65] The flattened elliptical cross-section of the P2VP cylinders is a result of shrinkage in the out-of-plane direction during deswelling.

Metal Exfiltration and Its Effect on Swelling Ratio. We now consider the reversibility of the metal infiltration process and its effects on the solvent swelling. Mun and co-workers showed that immersion in 3 wt % HCl for 30 min could unload infiltrated Pt from PS-*b*-P2VP copolymer thin films,[58] though the residual amount of Pt was not reported. Following this approach, films were infiltrated with Pt (using a range of conditions, which give SR = 2.01−2.56, Table 1) and then immersed in 9 wt % HCl for 1 h to remove the Pt. Subsequent solvent annealing gave SR = 2.5−2.7 for all of the metal infiltration conditions examined (Figure S2). This SR value is lower than that of the pristine film (SR = 2.89), indicating that acid immersion did not fully reverse the locking effects of metal infiltration. To explain this observation, we consider an annealed, unmetallized BCP film treated with 9 wt % HCl alone, *i.e.*, with no metal precursor (Figure 1a and Figure S3). The HCl treatment reduced the SR, but the SR was restored to that of the pristine film by treating with 0.1 wt % KOH for 30 min. This suggests that the suppression of the SR is due to protonation of the P2VP blocks by acid immersion, which increases their hydrophilicity[66−68] and reduces the subsequent uptake of chloroform. We therefore draw two conclusions. First, unloading a metal-infiltrated BCP with an acid solution does not reversibly recover the swelling behavior of the unmetallized film because the P2VP remains protonated even if some or all of the metal is removed, and second, protonation without metal infiltration can lock the structure (to some extent) and can be reversed by deprotonation with KOH.

Different solutions were used to unload the metal from the thin films infiltrated with 10 mM Na_2PtCl_4 in 9 wt % HCl, and the results are presented in Figure 1d. Treating with 0.1 wt % KOH gave similar SR to unloading in 9 wt % HCl; that is, the SR is still below that of the pristine BCP film, and the locking is not fully reversed. However, a solution of 0.05 wt % KOH + 0.5 wt % Na_2EDTA was highly effective in both unloading the metal and deprotonating the P2VP blocks. The swelling ratio returned to the same value as that of the pristine film (Table 2). KOH + Na_2EDTA immersion removed the mushroom-like surface structures, which indicate channels for metal infiltration (Figure S4).

XPS was utilized to measure the ratio of platinum to carbon in the metal-infiltrated and unloaded films. The XPS spectra are shown in Figure 3d, and the elemental ratios of Pt:C are displayed in Table 3. The ratio of Pt to vinylpyridine monomer was calculated at 0.83:1 for the metal-infiltrated film, decreasing to 0.15:1 after unloading with HCl. In contrast, the Pt signal is at or below the detection limit after unloading with KOH + Na_2EDTA, corresponding to a ratio of at most 0.03:1. The KOH + Na_2EDTA unloading therefore restores the surface morphology and the SR to those of the unmetallized BCP, as well as removing the Pt, making the metal infiltration process fully reversible. The reaction mechanism of the EDTA is not fully understood. $[PtCl_4]^{2-}$ is a stable species, and it is expected to be difficult for the Cl^- ligands to exchange for P2VP blocks or EDTA.[69,70] However, the results indicate that Na_2EDTA is necessary to fully restore

https://doi.org/10.1021/acsnano.3c00723
ACS Nano 2023, 17, 12225−12233

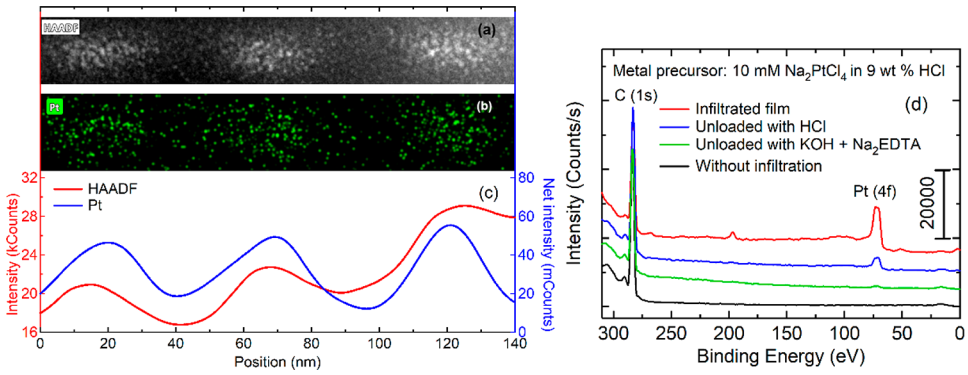

Figure 3. Distribution and content of metal in PS-*b*-P2VP block copolymer thin films: (a) STEM HAADF image, (b) STEM EDS image of Pt, (c) profile of HAADF and Pt intensity, and (d) XPS spectra after C_{60} sputtering. The horizontal axis of (c) gives the length scale for (a) and (b).

Table 2. Fitting Parameters of Swelling Ratio after Unloading Metal from the Films Infiltrated Using 10 mM Na_2PtCl_4 in 9 wt % HCl[a]

Unloading solution	$A + 1$	τ	β
9 wt % HCl	2.56	1009	1.39
0.1 wt % KOH	2.62	998	1.61
0.05 wt % KOH + 0.5 wt % Na_2EDTA	2.84	1117	1.62

[a]The R^2 of every fitting is higher than 0.99.

Table 3. Atomic Percent of Carbon and Platinum and the Corresponding Monomer Ratio

Sample	Pt (%)	C (%)	Pt:2VP monomer
Infiltrated film	3.31	96.69	0.83:1
Unloaded with HCl	0.63	99.37	0.15:1
Unloaded with KOH + Na_2EDTA	0.13	99.87	0.03:1

the swelling ratio. We speculate that the replacement of Cl^- ligands by EDTA is promoted at high pH, and the EDTA-Pt complex and remaining Na_2EDTA are then removed after washing with deionized water, as demonstrated in Figure S7.

Locking, Unlocking, and Morphology Cycling. The reversibility of metal infiltration enables control over the swelling ratio and hence the morphology of the BCP microdomains, as illustrated schematically in Figure 4 and experimentally in Figure 5. First, three identical as-cast films (stage 1) were annealed by the constant flow method (SR = 2.89) and deswelled to produce a single layer of in-plane P2VP cylinders (stage 2). They then underwent different processes, *i.e.*, without infiltration, treated with 9 wt % HCl, and infiltrated with 10 mM Pt in 9 wt % HCl, respectively. Then the three films were annealed using the reservoir method (Methods) (stage 3), which produces a higher swelling ratio than the constant flow method and, hence, a different microdomain morphology. The resulting structures (after deswelling) were infiltrated with Pt, then etched, and imaged to reveal their morphologies (stage 4).

The swelling ratios and morphologies of the three films at stage 4 are shown in Figure 5. For the film without infiltration (no locking effect), the swelling ratio in the reservoir annealing process was 3.46, and a mixture of in-plane and out-of-plane oriented cylindrical microdomains was produced (Figure 5b). This shows that the second annealing process at higher SR converted the in-plane cylinders to a mixed orientation. The film that was treated with 9 wt % HCl only (providing a weak locking effect) had SR = 3.25 in the reservoir annealing process, and this amount of solvent uptake converted the morphology to a double layer of in-plane cylindrical microdomains (Figure 5c). The cylinders in each layer are parallel and offset from each other. Finally, the film that was metallized (strong locking effect) exhibits SR = 2.84 in the reservoir

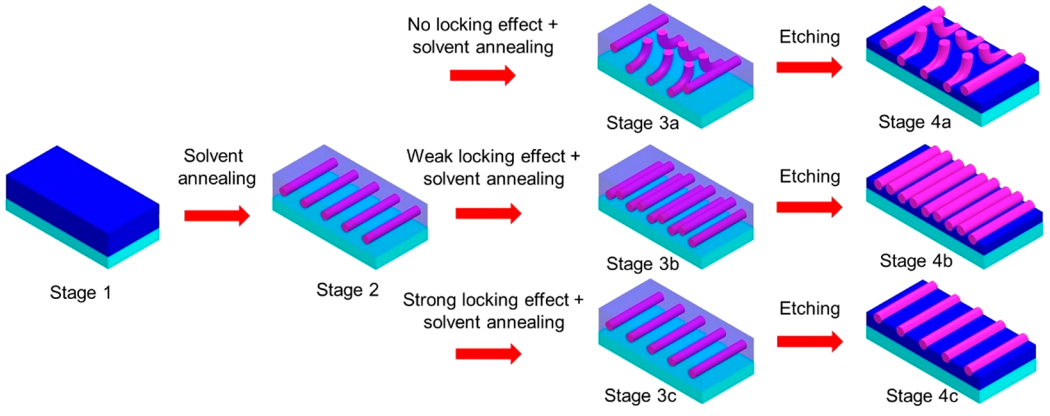

Figure 4. Schematic illustration of the morphologies of PS-*b*-P2VP thin films after different processing treatments. stage 1: as-cast PS-*b*-P2VP thin film with a thickness of 37 nm; stage 2: constant flow solvent annealing (SR = 2.89) to form in-plane cylindrical structures; stage 3: thin films undergoing different locking processes followed by annealing using the reservoir method (SR = 3.46, 3.25, and 2.84, respectively); and stage 4: metal infiltration followed by oxygen plasma etching.

https://doi.org/10.1021/acsnano.3c00723
ACS Nano 2023, 17, 12225−12233

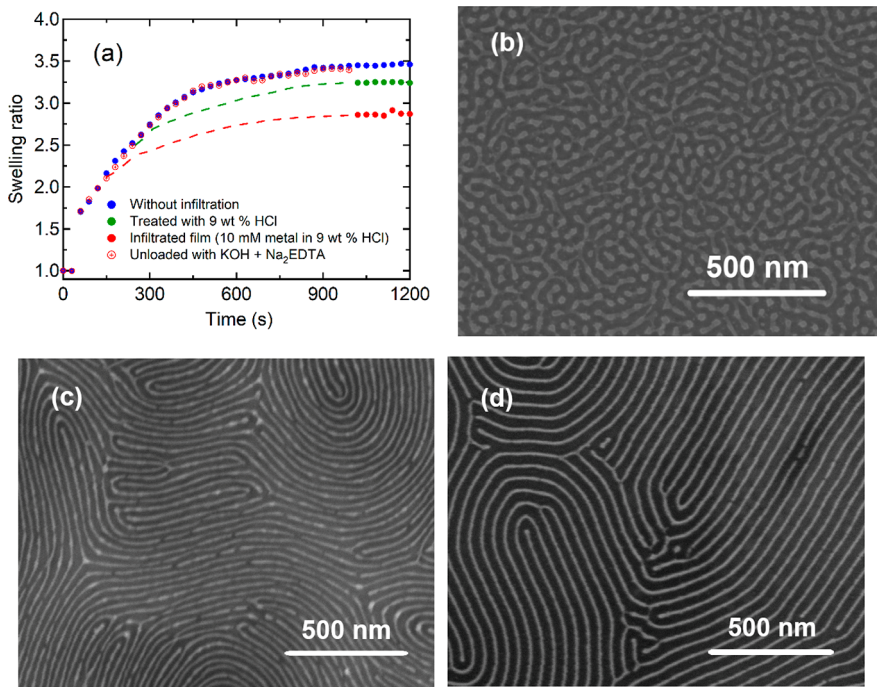

Figure 5. Swelling ratio and morphologies of different PS-*b*-P2VP thin films simultaneously processed using reservoir annealing. (a) Swelling ratio of the thin films. The first three were annealed together, and the SR of only one of them could be measured for times below 1000 s. Schematic dashed lines are shown for the other two. The fourth data set is from a separate measurement. Morphologies of (b) film without infiltration (stage 4a), (c) film treated with 9 wt % HCl (stage 4b), (d) infiltrated film (stage 4c) with morphology unchanged from stage 2.

annealing process, and the morphology remained as a single layer of in-plane cylindrical microdomains after reservoir annealing (Figure 5d).

The morphology depends on the annealing process because at a lower SR the differences in interface energies of the blocks dominate the orientation, promoting in-plane structures.[28,55] An out-of-plane orientation is preferred at high SR due to the gradient of solvent concentration through the film thickness.[28,55,71] In our 37 nm thick film, SR = 2.84 produced single-layer in-plane cylinders, SR = 3.25 produced double-layer in-plane cylinders, and SR = 3.46 produced mixed-orientation cylinders. The pristine unlocked film can transition between these structures when reannealed, whereas the metallized, locked film cannot.

Unloading the metal from the films allowed for reversibility of the morphology changes. An exemplary morphology cycle is presented in Figure 6. Initially, the constant flow annealing process generated single-layer in-plane cylindrical microdomains (Figure 6a). Metal infiltration locked the structures, so the reservoir annealing did not affect the morphology, and single-layer cylinders remained (Figure 6b). But after unloading the metal and deprotonating with KOH + Na_2EDTA, the behavior of the unloaded film reverted to that of the pristine unmetallized film, and a subsequent reservoir annealing step yielded mixed-orientation cylinders at high SR (Figure 6c). After the metal was infiltrated, the mixed-orientation cylinders could be locked and preserved (Figure 6d) during a subsequent reservoir annealing. However, if the metal is unloaded, constant flow annealing for 1 h transforms the mixed-orientation cylinders back to the initial in-plane single-layer features (Figure 6e).

The reversibility of metal infiltration and morphology change was also demonstrated for another metal, iron, from a $K_3Fe(CN)_6$ precursor solution. After unloading iron by KOH + Na_2EDTA, solvent uptake was restored, and the morphology was unlocked (Figure S5). The quality of iron patterns is lower than that of platinum patterns due to the lower stability of the Fe nanostructures during etching.[24]

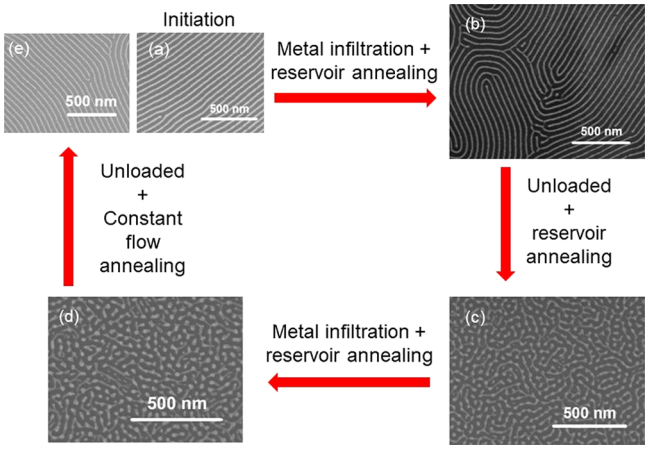

Figure 6. Morphology cycle of a PS-*b*-P2VP thin film, showing how the morphology varies with combinations of locking (via metallization) and unlocking (via KOH + Na_2EDTA) and the two annealing processes. (a) An as-cast film exhibits in-plane cylindrical microdomains after constant flow annealing. (b) In-plane cylinders were preserved in a subsequent reservoir annealing step after metal infiltration, because the film morphology was locked. (c) After unloading the metal and unlocking the morphology, reservoir annealing yielded mixed-orientation cylinders. (d) After infiltrating metal, the mixed-orientation cylinders were locked and remained after subsequent reservoir annealing. (e) After unlocking, 1 h constant flow annealing converted the mixed-orientation cylinders back to the initial in-plane cylindrical structure.

https://doi.org/10.1021/acsnano.3c00723
ACS Nano 2023, 17, 12225−12233

The reversibility of metal infiltration provides a useful tool for complex structure design by loading or unloading metal in specific regions of the film. For example, we prepared a film with single-layer in-plane cylinders using the constant flow process and metallized it (stage 3c), then unloaded the metal from one region (defined by the meniscus of the KOH + Na_2EDTA unloading solution), and then reannealed the sample in the reservoir process. This treatment yields different morphologies in the two distinct regions separated by a transition zone, varying between those of stage 4a through stage 4b and stage 4c over a distance of 2 μm (Figure S6).

The KOH + Na_2EDTA solution provides superior reversibility compared to 0.05 or 0.1 wt % KOH solutions. If the Pt is unloaded in KOH alone, SR is not fully recovered, and a subsequent reservoir annealing process converts the single layer in-plane cylinders to double-layer cylindrical microdomains rather than to mixed-orientation cylinders, as shown in Figure S8.

Constructing non-native 3D morphologies in multilayer BCP thin films has been the focus of recent research.[41,72] For example, irreversible locking of the bottom layer via sequential infiltration synthesis was used to make non-native polystyrene-block-poly(methylmethacrylate) structures,[72] whereas various complex 3D structures were produced using nonequilibrium processing pathways without locking.[73] The ability of reversible metal infiltration to lock the structure against subsequent morphological changes and then unlock it to allow changes could facilitate the further development of multilevel 3D structures in which the morphology of underlying layers of BCP needs to be stabilized during the spin coating and then to be recovered in the subsequent evolution pathway. We will demonstrate the application of metal infiltration and exfiltration on the design of 3D non-native structures in a future study.

CONCLUSIONS

This work demonstrates the interplay among metal infiltration, metal exfiltration, solvent swelling, and morphology in a PS-*b*-P2VP diblock copolymer thin film. Pt is infiltrated into the P2VP microdomains from an acidic solution of platinate(II), and the resulting Pt content approaches 0.83 Pt atom per pyridine group for the infiltration solution with the highest acid and metal salt concentrations. Metal infiltration provides a locking effect on the self-assembled microdomain morphology, lowering the swelling ratio and inhibiting reorganization of the morphology during a subsequent solvent annealing step. The suppression of the swelling ratio is attributed to electrostatic charging of the P2VP block that lowers solvent uptake and chain mobility; even treatment in HCl solution without metal precursor suppresses swelling and provides a weak locking effect.

A solution of KOH + Na_2EDTA is more effective than HCl or KOH solutions in exfiltrating the Pt, with residual Pt content below the detection limit of 0.03 Pt/pyridine unit. Exfiltration unlocks the morphology, restoring the swelling ratio to that of the as-cast film and allowing morphology changes to occur when the solvent annealing conditions are modified. The reversible locking and unlocking process developed here offers a method for building up a 2D or 3D structure in a multistep process, diversifying the toolkit for BCP-enabled nanofabrication.

EXPERIMENTAL METHODS

The PS-*b*-P2VP BCP was purchased from Polymer Source Inc. The number-average molecular weights (M_n) of the PS block and P2VP block were 79.0 and 36.5 kg/mol, respectively (f_{P2VP} = 31.6%), and the dispersity was 1.05. The BCP was dissolved 1 wt % in toluene and spin-coated on an oxidized silicon substrate at 3.0 krpm. The resulting thickness was 37 ± 2 nm, determined with a Filmetrics F20 spectral reflectometer. The films were annealed in a 5 cm diameter × 5 cm height cylindrical glass chamber with a 10 sccm flow of chloroform vapor produced by bubbling nitrogen gas through liquid chloroform for 30 min (named the *constant flow annealing method*)[74] to form ordered structures. Thereafter a 200 sccm nitrogen flow for 5 min is used to deswell the film, controlled by a mass flow controller. A second process (named the *reservoir method*) consists of annealing the sample in the same sized cylindrical chamber containing 1 mL of chloroform solvent and a 1.9 sccm nitrogen gas flow for 20 min. The reservoir method exposes the sample to a higher vapor pressure of solvent, leading to a higher swelling ratio with faster rise time. The solubility parameters of chloroform, PS, and P2VP are 18.9,[75] 18.4,[75] and 21.2,[76] respectively, indicating that chloroform is selective to PS and preferentially swells the PS block. The solubility parameters are given in Table S1.

For metallization, Na_2PtCl_4 was purchased from Sigma-Aldrich as the platinum metal precursor. The precursor was dissolved in HCl aqueous solution with different Pt concentrations (10, 5, and 1 mM) and acid concentrations (9, 0.9, and 0.09 wt % HCl). The solution was dripped on the annealed thin films and covered the surface for 30 min at room temperature. Then, the films were washed with deionized water and blown dry by nitrogen gas to remove residual water. To remove metal from infiltrated films, we use solutions containing ethylenediaminetetraacetic acid disodium salt dihydrate (Na_2EDTA) purchased from Sigma-Aldrich. A 9 wt % HCl aqueous solution, a 0.1 wt % KOH aqueous solution, and a mixed aqueous solution of KOH (0.05 wt %) and Na_2EDTA (0.5 wt %) were dripped on the center of the metallized films for 60, 30, and 30 min, respectively. The subsequent washing and drying processes were the same as those used for the metallization process. A solution of 10 mM $K_3Fe(CN)_6$ in 9 wt % HCl was used for Fe infiltration.

A Filmetrics F20 spectral reflectometer was used to measure the thickness of the films during the solvent annealing. The swelling ratio vs time (t) was fitted by the stretched exponential or Kohlrausch–Williams–Watts function:[77,78]

$$\mathrm{SR} = A\left(1 - \exp\left(-\left(\frac{t}{\tau}\right)^{\beta}\right)\right) + 1$$

where A + 1 is the plateau value of the swelling ratio, τ is a characteristic time to reach equilibrium, and β is the shape factor, indicating the width of the SR function.[62−64]

A Physical Electronics Versaprobe II X-ray photoelectron spectrometer (XPS) was used to analyze the platinum content inside metallized and demetallized films. The top surface of the films was cleaned by a C_{60} cluster-ion gun (10 kV voltage and 5 nA current) for 1 min. A Thermo Fisher Scientific Themis Z G3 aberration-corrected scanning transmission electron microscope (STEM) with energy dispersive X-ray spectroscopy (EDS) was used to characterize the metallized film in cross-section and to qualitatively image the Pt distribution. To prepare the STEM sample, a protective layer of 50 nm carbon was coated on the metal-infiltrated film, followed by depositing a Pt protective layer on the top. Then, the film was cut by a Raith VELION focused ion beam (FIB) and imaged by scanning electron microscope (SEM), and the resulting sample was welded to a TEM grid.

Oxygen plasma etching (6 mTorr pressure, 10 sccm gas flow, and 90 W power) was carried out to selectively remove the PS block for 7 s, converting the Pt-infiltrated P2VP block into a metal-rich nanostructure.[55] The morphologies of etched samples were imaged by a Zeiss Merlin SEM or a Zeiss Gemini 450 SEM under 3 kV.

https://doi.org/10.1021/acsnano.3c00723
ACS Nano 2023, 17, 12225−12233

ASSOCIATED CONTENT

Supporting Information

The Supporting Information is available free of charge at https://pubs.acs.org/doi/10.1021/acsnano.3c00723.

Figure of swelling ratio fitting, figure of swelling ratio plateau after unloading with acid, figure of swelling ratio after restoring with base, AFM images of surface topography, SEM images of morphologies after solvent annealing, SEM images of localized unlocking morphology, XPS spectra for remaining Na_2EDTA, and SEM images of incomplete morphology unlocking by KOH (PDF)

AUTHOR INFORMATION

Corresponding Author

Caroline A. Ross − *Department of Materials Science and Engineering, Massachusetts Institute of Technology, Cambridge, Massachusetts 02139, United States;* orcid.org/0000-0003-2262-1249; Email: caross@mit.edu

Authors

Mingchao Ma − *Department of Materials Science and Engineering, Massachusetts Institute of Technology, Cambridge, Massachusetts 02139, United States;* orcid.org/0000-0003-4563-7542

Runze Liu − *Department of Materials Science and Engineering, Massachusetts Institute of Technology, Cambridge, Massachusetts 02139, United States;* orcid.org/0000-0001-6040-6940

Tingyu Su − *Department of Materials Science and Engineering, Massachusetts Institute of Technology, Cambridge, Massachusetts 02139, United States;* orcid.org/0000-0002-1154-2855

Zehao Sun − *Department of Materials Science and Engineering, Massachusetts Institute of Technology, Cambridge, Massachusetts 02139, United States;* orcid.org/0000-0002-9720-694X

Complete contact information is available at: https://pubs.acs.org/10.1021/acsnano.3c00723

Notes

The authors declare no competing financial interest.

ACKNOWLEDGMENTS

We acknowledge a Postdoctoral Fellowship from Shanghai Jiao Tong University and support from NSF DMREF award 2218678. This work was performed in part on the Raith VELION FIB-SEM in the MIT.nano Characterization Facilities under Award DMR-2117609.

REFERENCES

(1) Tavakkoli, K. G. A.; Gotrik, K. W.; Hannon, A. F.; Alexander-Katz, A.; Ross, C. A.; Berggren, K. K. Templating Three-Dimensional Self-Assembled Structures in Bilayer Block Copolymer Films. *Science* **2012**, *336*, 1294−1298.

(2) Kim, S. O.; Solak, H. H.; Stoykovich, M. P.; Ferrier, N. J.; Pablo, J. J. d.; Nealey, P. F. Epitaxial Self-assembly of Block Copolymers on Lithographically Defined Nanopatterned Substrates. *Nature* **2003**, *424*, 411−414.

(3) Tang, C.; Lennon, E. M.; Fredrickson, G. H.; Kramer, E. J.; Hawker, C. J. Evolution of Block Copolymer Lithography to Highly Ordered Square Arrays. *Science* **2008**, *322*, 429−432.

(4) Ruiz, R.; Kang, H.; Detcheverry, F. A.; Dobisz, E.; Kercher, D. S.; Albrecht, T. R.; Pablo, J. J. d.; Nealey, P. F. Density Multiplication and Improved Lithography by Directed Block Copolymer Assembly. *Science* **2008**, *321*, 936−939.

(5) Ross, C. A.; Berggren, K. K.; Cheng, J. Y.; Jung, Y. S.; Chang, J.-B. Three-Dimensional Nanofabrication by Block Copolymer Self-Assembly. *Adv. Mater.* **2014**, *26*, 4386−4396.

(6) Darling, S. B. Directing the self-assembly of block copolymers. *Prog. Polym. Sci.* **2007**, *32*, 1152−1204.

(7) Kim, J. K.; Yang, S. Y.; Lee, Y.; Kim, Y. Functional Nanomaterials Based on Block Copolymer Self-assembly. *Prog. Polym. Sci.* **2010**, *35*, 1325−1349.

(8) Kim, H.-C.; Hinsberg, W. D. Surface Patterns from Block Copolymer Self-assembly. *J. Vac. Sci. Technol. A* **2008**, *26*, 1369−1382.

(9) Dinachali, S. S.; Bai, W.; Tu, K.-H.; Choi, H. K.; Zhang, J.; Kreider, M. E.; Cheng, L.-C.; Ross, C. A. Thermo-Solvent Annealing of Polystyrene-Polydimethylsiloxane Block Copolymer Thin Films. *ACS Macro Lett.* **2015**, *4*, 500−504.

(10) Gu, X.; Gunkel, I.; Hexemer, A.; Russell, T. P. Controlling Domain Spacing and Grain Size in Cylindrical Block Copolymer Thin Films by Means of Thermal and Solvent Vapor Annealing. *Macromolecules* **2016**, *49*, 3373−3381.

(11) Campbell, I. P.; He, C.; Stoykovich, M. P. Topologically Distinct Lamellar Block Copolymer Morphologies Formed by Solvent and Thermal Annealing. *ACS Macro Lett.* **2013**, *2*, 918−923.

(12) Guarini, K. W.; Black, C. T.; Yeung, S. H. I. Optimization of Diblock Copolymer Thin FilmSelf Assembly. *Adv. Mater.* **2002**, *14*, 1290−1294.

(13) Knoll, A.; Horvat, A.; Lyakhova, K. S.; Krausch, G.; Sevink, G. J. A.; Zvelindovsky, A. V.; Magerle, R. Phase Behavior in Thin Films of Cylinder-Forming Block Copolymers. *Phys. Rev. Lett.* **2002**, *89*, 035501.

(14) Brassat, K.; Kool, D.; Nallet, C. G. A.; Lindner, J. K. N. Understanding Film Thickness-Dependent Block Copolymer Self-Assembly by Controlled Polymer Dewetting on Prepatterned Surfaces. *Adv. Mater. Interfaces* **2020**, *7*, 1901605.

(15) Brassat, K.; Kool, D.; Bürger, J.; Lindner, J. K. N. Hierarchical nanopores formed by block copolymer lithography on the surfaces of different materials pre-patterned by nanosphere lithography. *Nanoscale* **2018**, *10*, 10005−10017.

(16) Han, E.; Stuen, K. O.; Leolukman, M.; Liu, C.-C.; Nealey, P. F.; Gopalan, P. Perpendicular Orientation of Domains in Cylinder-Forming Block Copolymer Thick Films by Controlled Interfacial Interactions. *Macromolecules* **2009**, *42*, 4896−4901.

(17) Pang, Y.; Wan, L.; Huang, G.; Zhang, X.; Jin, X.; Xu, P.; Liu, Y.; Han, M.; Wu, G.-P.; Ji, S. Controlling Block Copolymer-Substrate Interactions by Homopolymer Brushes/Mats. *Macromolecules* **2017**, *50*, 6733−6741.

(18) Jung, Y. S.; Jung, W.; Ross, C. A. Nanofabricated Concentric Ring Structures by Templated Self-Assembly of a Diblock Copolymer. *Nano Lett.* **2008**, *8*, 2975−2981.

(19) Ruiz, R.; Ruiz, N.; Zhang, Y.; Sandstrom, R. L.; Black, C. T. Local Defectivity Control of 2D Self-Assembled Block Copolymer Patterns. *Adv. Mater.* **2007**, *19*, 2157−2162.

(20) Cheng, J. Y.; Ross, C. A.; Thomas, E. L.; Smith, H. I.; Vancso, G. J. Templated Self-Assembly of Block Copolymers: Effect of Substrate Topography. *Adv. Mater.* **2003**, *15*, 1599−1602.

(21) Posselt, D.; Zhang, J.; Smilgies, D.-M.; Berezkin, A. V.; Potemkin, I. I.; Papadakis, C. M. Restructuring in Block Copolymer Thin Films: In Situ GISAXS Investigations During Solvent Vapor Annealing. *Prog. Polym. Sci.* **2017**, *66*, 80−115.

(22) Jin, C.; Olsen, B. C.; Luber, E. J.; Buriak, J. M. Nanopatterning via Solvent Vapor Annealing of Block Copolymer Thin Films. *Chem. Mater.* **2017**, *29*, 176−188.

(23) Shi, L.-Y.; Lee, S.; Du, Q.; Zhou, B.; Weng, L.; Liu, R.; Ross, C. A. Bending Behavior and Directed Self-Assembly of Rod-Coil Block Copolymers. *ACS Appl. Mater. Interfaces* **2021**, *13*, 10437−10445.

(24) Liu, R.; Huang, H.; Sun, Z.; Alexander-Katz, A.; Ross, C. A. Metallic Nanomeshes Fabricated by Multimechanism Directed Self-Assembly. *ACS Nano* **2021**, *15*, 16266−16276.
(25) Jeong, J. W.; Park, W. I.; Kim, M.-J.; Ross, C. A.; Jung, Y. S. Highly Tunable Self-Assembled Nanostructures from a Poly(2-vinylpyridine-b-dimethylsiloxane) Block Copolymer. *Nano Lett.* **2011**, *11*, 4095−4101.
(26) Tu, K.-H.; Huang, H.; Lee, S.; Lee, W.; Sun, Z.; Alexander-Katz, A.; Ross, C. A. Machine Learning Predictions of Block Copolymer Self-Assembly. *Adv. Mater.* **2020**, *32*, 2005713.
(27) Selkirk, A.; Prochukhan, N.; Lundy, R.; Cummins, C.; Gatensby, R.; Kilbride, R.; Parnell, A.; Vasquez, J. B.; Morris, M.; Mokarian-Tabari, P. Optimization and Control of Large Block Copolymer Self-Assembly via Precision Solvent Vapor Annealing. *Macromolecules* **2021**, *54*, 1203−1215.
(28) Bai, W.; Yager, K. G.; Ross, C. A. In Situ Characterization of the Self-Assembly of a Polystyrene-Polydimethylsiloxane Block Copolymer during Solvent Vapor Annealing. *Macromolecules* **2015**, *48*, 8574−8584.
(29) Cetintas, M.; Kamperman, M. Self-assembly of PS-b-PNIPAM-b-PS block copolymer thin films via selective solvent annealing. *Polymer* **2016**, *107*, 387−397.
(30) Chavis, M. A.; Smilgies, D.-M.; Wiesner, U. B.; Ober, C. K. Widely Tunable Morphologies in Block Copolymer Thin Films Through Solvent Vapor Annealing Using Mixtures of Selective Solvents. *Adv. Funct. Mater.* **2015**, *25*, 3057−3065.
(31) Jung, Y. S.; Ross, C. A. Solvent-Vapor-Induced Tunability of Self-Assembled Block Copolymer Patterns. *Adv. Mater.* **2009**, *21*, 2540−2545.
(32) Hulkkonen, H.; Salminen, T.; Niemi, T. Automated Solvent Vapor Annealing with Nanometer Scale Control of Film Swelling for Block Copolymer Thin Films. *Soft Matter* **2019**, *15*, 7909−7917.
(33) Tada, Y.; Yoshida, H.; Yoshihito, I.; Hirai, T.; Bosworth, J. K.; Dobisz, E.; Ruiz, R.; Takenaka, M.; Hayakawa, T.; Hasegawa, H. Directed Self-Assembly of POSS Containing Block Copolymer on Lithographically Defined Chemical Template with Morphology Control by Solvent Vapor. *Macromolecules* **2012**, *45*, 292−304.
(34) Nelson, G.; Drapes, C. S.; Grant, M. A.; Gnabasik, R.; Wong, J.; Baruth, A. High-Precision Solvent Vapor Annealing for Block Copolymer Thin Films. *Micromachines* **2018**, *9*, 271.
(35) Kim, J. M.; Kim, Y.; Park, W. I.; Hur, Y. H.; Jeong, J. W.; Sim, D. M.; Baek, K. M.; Lee, J. H.; Kim, M.-J.; Jung, Y. S. Eliminating the Trade-Off between the Throughput and Pattern Quality of Sub-15 nm Directed Self-Assembly via Warm Solvent Annealing. *Adv. Funct. Mater.* **2015**, *25*, 306−315.
(36) Gotrik, K. W.; Ross, C. A. Solvothermal Annealing of Block Copolymer Thin Films. *Nano Lett.* **2013**, *13*, 5117−5122.
(37) Park, W. I.; Kim, K.; Jang, H.-I.; Jeong, J. W.; Kim, J. M.; Choi, J.; Park, J. H.; Jung, Y. S. Directed Self-Assembly with Sub-100 Degrees Celsius Processing Temperature, Sub-10 Nanometer Resolution, and Sub-1 minute Assembly Time. *Small* **2012**, *8*, 3762−3768.
(38) Stahl, B. C.; Kramer, E. J.; Hawker, C. J.; Lynd, N. A. Controlled Co-Solvent Vapor Annealing and the Importance of Quenching Conditions in Thin-Film Block Copolymer Self-Assembly. *J. Polym. Sci. B Polym. Phys.* **2017**, *55*, 1125−1130.
(39) Choi, S. Y.; Lee, C.; Lee, J. W.; Park, C.; Kim, S. H. Dewetting-Induced Hierarchical Patterns in Block Copolymer Films. *Macromolecules* **2012**, *45*, 1492−1498.
(40) Zhang, X.; Metting, C. J.; Briber, R. M.; Weilnboeck, F.; Shin, S. H.; Jones, B. G.; Oehrlein, G. S. Poly(2-vinylnaphthalene)-block-poly(acrylic acid) Block Copolymer: Self-Assembled Pattern Formation, Alignment, and Transfer into Silicon via Plasma Etching. *Macromol. Chem. Phys.* **2011**, *212*, 1735−1741.
(41) Oh, J.; Suh, H. S.; Ko, Y.; Nah, Y.; Lee, J.-C.; Yeom, B.; Char, K.; Ross, C. A.; Son, J. G. Universal Perpendicular Orientation of Block Copolymer Microdomains Using a Filtered Plasma. *Nat. Commun.* **2019**, *10*, 2912.
(42) Son, J. G.; Chang, J.-B.; Berggren, K. K.; Ross, C. A. Assembly of Sub-10-nm Block Copolymer Patterns with Mixed Morphology and Period Using Electron Irradiation and Solvent Annealing. *Nano Lett.* **2011**, *11*, 5079−5084.
(43) Arora, H.; Du, P.; Tan, K. W.; Hyun, J. K.; Grazul, J.; Xin, H. L.; Muller, D. A.; Thompson, M. O.; Wiesner, U. Block Copolymer Self-Assembly-Directed Single-Crystal Homo- and Heteroepitaxial Nanostructures. *Science* **2010**, *330*, 214−219.
(44) Bosworth, J. K.; Black, C. T.; Ober, C. K. Selective Area Control of Self-Assembled Pattern Architecture Using a Lithographically Patternable Block Copolymer. *ACS Nano* **2009**, *3*, 1761−1766.
(45) Chan, N.; Yee, N.; An, S. Y.; Oh, J. K. Tuning Amphiphilicity/Temperature-Induced Self-Assembly and In-Situ Disulfide Crosslinking of Reduction-Responsive Block Copolymers. *J. Polym. Sci. A Polym. Chem.* **2014**, *52*, 2057−2067.
(46) Kamcev, J.; Germack, D. S.; Nykypanchuk, D.; Grubbs, R. B.; Nam, C.-Y.; Black, C. T. Chemically Enhancing Block Copolymers for Block-Selective Synthesis of Self-Assembled Metal Oxide Nanostructures. *ACS Nano* **2013**, *7*, 339−346.
(47) Bosworth, J. K.; Paik, M. Y.; Ruiz, R.; Schwartz, E. L.; Huang, J. Q.; Ko, A. W.; Smilgies, D.-M.; Black, C. T.; Ober, C. K. Control of Self-Assembly of Lithographically Patternable Block Copolymer Films. *ACS Nano* **2008**, *7*, 1396−1402.
(48) Chai, J.; Wang, D.; Fan, X.; Buriak, J. M. Assembly of aligned linear metallic patterns on silicon. *Nat. Nanotechnol.* **2007**, *2*, 500−506.
(49) Shin, D. O.; Lee, D. H.; Moon, H.-S.; Jeong, S.-J.; Kim, J. Y.; Mun, J. H.; Cho, H.; Park, S.; Kim, S. O. Sub-Nanometer Level Size Tuning of a Monodisperse Nanoparticle Array Via Block Copolymer Lithography. *Adv. Funct. Mater.* **2011**, *21*, 250−254.
(50) Kim, J. J.; Suh, H. S.; Zhou, C.; Mane, A. U.; Lee, B.; Kim, S.; Emery, J. D.; Elam, J. W.; Nealey, P. F.; Fenter, P.; Fister, T. T. Mechanistic Understanding of Tungsten Xxide In-plane Nanostructure Growth via Sequential Infiltration Synthesis. *Nanoscale* **2018**, *10*, 3469−3479.
(51) Wu, N. L. Y.; Zhang, X.; Murphy, J. N.; Chai, J.; Harris, K. D.; Buriak, J. M. Density Doubling of Block Copolymer Templated Features. *Nano Lett.* **2012**, *12*, 264−268.
(52) Chai, J.; Buriak, J. M. Using Cylindrical Domains of Block Copolymers To Self-Assemble and Align Metallic Nanowires. *ACS Nano* **2008**, *2*, 489−501.
(53) Cummins, C.; Gangnaik, A.; Kelly, R. A.; Borah, D.; O'Connell, J.; Petkov, N.; Georgiev, Y. M.; Holmes, J. D.; Morris, M. A. Aligned silicon nanofins via the directed selfassembly of PS-b-P4VP block copolymer and metal oxide enhanced pattern transfer. *Nanoscale* **2015**, *7*, 6712−6721.
(54) Shin, D. O.; Mun, J. H.; Hwang, G.-T.; Yoon, J. M.; Kim, J. Y.; Yun, J. M.; Yang, Y.-B.; Oh, Y.; Lee, J. Y.; Shin, J.; Lee, K. J.; Park, S.; Kim, J. U.; Kim, S. O. Multicomponent Nanopatterns by Directed Block Copolymer Self-Assembly. *ACS Nano* **2013**, *7*, 8899−8907.
(55) Lee, W.; Lee, S.; Tang, A. S.; Kim, C.; Liu, R.; Im, K.; Jung, H.-T.; Ross, C. A. Platinum Infiltration of a Block Copolymer for Interconnected Three-Dimensional Metal Nanostructures. *ACS Appl. Nano Mater.* **2021**, *4*, 793−801.
(56) Aizawa, M.; Buriak, J. M. Block Copolymer Templated Chemistry for the Formation of Metallic Nanoparticle Arrays on Semiconductor Surfaces. *Chem. Mater.* **2007**, *19*, 5090−5101.
(57) Kennemur, J. G. Poly(vinylpyridine) Segments in Block Copolymers: Synthesis, Self-Assembly, and Versatility. *Macromolecules* **2019**, *52*, 1354−1370.
(58) Mun, J. H.; Cha, S. K.; Kim, Y. C.; Yun, T.; Choi, Y. J.; Jin, H. M.; Lee, J. E.; Jeon, H. U.; Kim, S. Y.; Kim, S. O. Controlled Segmentation of Metal Nanowire Array by Block Copolymer Lithography and Reversible Ion Loading. *Small* **2017**, *13*, 1603939.
(59) Cha, S. K.; Lee, G. Y.; Mun, J. H.; Jin, H. M.; Moon, C. Y.; Kim, J. S.; Kim, K. H.; Jeong, S.-J.; Kim, S. O. Self-Assembly of Complex Multimetal Nanostructures from Perforated Lamellar Block

https://doi.org/10.1021/acsnano.3c00723
ACS Nano 2023, 17, 12225−12233

Copolymer Thin Films. *ACS Appl. Mater. Interfaces* **2017**, *9*, 15727−15732.
(60) Cha, S. K.; Mun, J. H.; Chang, T.; Kim, S. Y.; Kim, J. Y.; Jin, H. M.; Lee, J. Y.; Shin, J.; Kim, K. H.; Kim, S. O. Au-Ag Core-Shell Nanoparticle Array by Block Copolymer Lithography for Synergistic Broadband Plasmonic Properties. *ACS Nano* **2015**, *9*, 5536−5543.
(61) Mun, J. H.; Cha, S. K.; Kim, H.; Moon, H.-S.; Kim, J. Y.; Jin, H. M.; Choi, Y. J.; Baek, J. E.; Shin, J.; Kim, S. O. Nanodomain Swelling Block Copolymer Lithography for Morphology Tunable Metal Nanopatterning. *Small* **2014**, *10*, 3742−3749.
(62) O'Connell, P. A.; McKenna, G. B. Arrhenius-type temperature dependence of the segmental relaxation below Tg. *J. Chem. Phys.* **1999**, *110*, 11054−11060.
(63) Shi, X.; Mandanici, A.; McKenna, G. B. Shear Stress Relaxation and Physical Aging Study on Simple Glass-forming Materials. *J. Chem. Phys.* **2005**, *123*, 174507.
(64) Wortmann, F. J.; Stapels, M.; Chandra, L. Humidity-Dependent Bending Recovery and Relaxation of Human Hair. *J. Appl. Polym. Sci.* **2009**, *113*, 3336−3344.
(65) Subramanian, A.; Tiwale, N.; Doerk, G.; Kisslinger, K.; Nam, C.-Y. Enhanced Hybridization and Nanopatterning via Heated Liquid-Phase Infiltration into Self-Assembled Block Copolymer Thin Films. *ACS Appl. Mater. Interfaces* **2020**, *12*, 1444−1453.
(66) Liu, Y.; Cui, X.; Lee, Y.-I.; Liu, H.-G. Self-Assembly of Polystyrene-b-poly(2-vinylpyridine)/Chloroauric Acid at the Liquid/Liquid Interface. *Langmuir* **2022**, *38*, 4589−4598.
(67) Iatridi, Z.; Roiter, Y.; Stavrouli, N.; Minko, S.; Tsitsilianis, C. Phase Behavior and Self-assembly of PSn(P2VP-b-PAA)n Multiarmed Multisegmented Star Terpolymers with Ampholytic arms. *Polym. Chem.* **2011**, *2*, 2037−2044.
(68) Butsele, K. V.; Fustin, C. A.; Gohy, J. F.; Jérôme, R.; Jérôme, C. Self-Assembly and pH-Responsiveness of ABC Miktoarm Star Terpolymers. *Langmuir* **2009**, *25*, 25.
(69) Ayres, G. H.; Glass, P. W. The EDTA complex of platinum (IV): a titrimetric and spectrophotometric study. *Anal. Chim. Acta* **1972**, *60*, 357−365.
(70) Stehr, J. e.; Lundström, I.; Karlsson, J. O. Evidence that Fodipir (DpDp) Binds Neurotoxic pt^{2+} with a High Affinity: An Electron Paramagnetic Resonance Study. *Sci. Rep.* **2019**, *9*, 15813.
(71) Kim, S. H.; Misner, M. J.; Xu, T.; Kimura, M.; Russell, T. P. Highly Oriented and Ordered Arrays from Block Copolymers via Solvent Evaporation. *Adv. Mater.* **2004**, *16*, 226−231.
(72) Rahman, A.; Majewski, P. W.; Doerk, G.; Black, C. T.; Yager, K. G. Non-native Three-dimensional Block Copolymer Morphologies. *Nat. Commun.* **2016**, *7*, 13988.
(73) Russell, S. T.; Bae, S.; Subramanian, A.; Tiwale, N.; Doerk, G.; Nam, C.-Y.; Fukuto, M.; Yager, K. G. Priming Self-assembly Pathways by Stacking Block Copolymers. *Nat. Commun.* **2022**, *13*, 6947.
(74) Gotrik, K. W.; Hannon, A. F.; Son, J. G.; Keller, B.; Alexander-Katz, A.; Ross, C. A. Morphology Control in Block Copolymer Films Using Mixed Solvent Vapors. *ACS Nano* **2012**, *6*, 8052−8059.
(75) Mieczkowski, R. The Determination of the Solubility Parameter Components of Polystyrene. *Eur. Polym. J.* **1989**, *25*, 1055−1057.
(76) Arras, M. M. L.; He, B.; Jandt, K. D. High molar mass amphiphilic block copolymer enables alignment and dispersion of unfunctionalized carbon nanotubes in melt-drawn thin-films. *Polymer* **2017**, *127*, 15−27.
(77) Kohlrausch, R. Theorie des elektrischen Rückstandes in der Leidener Flasche. *Ann. Phys* **1854**, *162*, 179−214.
(78) Williams, G.; Watts, D. C. Non-symmetrical Dielectric Relaxation Behaviour Arising from a Simple Empirical Decay Function. *Trans. Faraday Soc.* **1970**, *66*, 80−85.

https://doi.org/10.1021/acsnano.3c00723
ACS Nano 2023, 17, 12225−12233